9-2009

Experimental and Theoretical Investigation of Molecular Field Effects by Polarization-resolved Resonant Inelastic X-ray Scattering

Stephane Carniato
Laboratory of Physical Chemistry - Matter and Radiation

Renaud Guillemin
CNRS, Laboratoire de Chimie Physique-Matière et Rayonnement

Wayne C. Stolte
University of Nevada, Las Vegas, wcstolte@lbl.gov

Loic Journel
Laboratory of Physical Chemistry - Matter and Radiation

Richard Taieb
Laboratory of Physical Chemistry - Matter and Radiation

Follow this and additional works at: https://digitalscholarship.unlv.edu/chem_fac_articles

Part of the Analytical Chemistry Commons, Atomic, Molecular and Optical Physics Commons, Biological and Chemical Physics Commons, and the Physical Chemistry Commons

See next page for additional authors

Authors

Stephane Carniato, Renaud Guillemin, Wayne C. Stolte, Loic Journel, Richard Taieb, Dennis W. Lindle, and Marc Simon

Experimental and theoretical investigation of molecular field effects by polarization-resolved resonant inelastic x-ray scattering

S. Carniato,[1] R. Guillemin,[1,2] W. C. Stolte,[3,4] L. Journel,[1] R Taïeb,[1,2] D. W. Lindle,[3] and M. Simon[1,2]

[1]*Laboratoire de Chimie Physique-Matière et Rayonnement, Université Pierre et Marie Curie, UMR 7614, 11 Rue Pierre et Marie Curie, 75231 Paris Cedex 05, France*

[2]*CNRS, Laboratoire de Chimie Physique-Matière et Rayonnement, UMR 7614, 11 Rue Pierre et Marie Curie, 75231 Paris Cedex 05, France*

[3]*Department of Chemistry, University of Nevada, Las Vegas, Nevada 89154-4003, USA*

[4]*Advanced Light Source, Lawrence Berkeley National Laboratory, Berkeley, California 94720, USA*

We present a combined theoretical and experimental study of molecular field effects on molecular core levels. Polarization-dependent resonant inelastic x-ray scattering is observed experimentally after resonant K-shell excitation of CF_3Cl and HCl. We explain the linear dichroism observed in spin-orbit level intensities as due to molecular field effects, including singlet-triplet exchange, and interpret this behavior in terms of population differences in the $2p_{x,y,z}$ inner-shell orbitals. We investigate theoretically the different factors that can affect the electronic populations and the dynamical R dependence of the spin-orbit ratio. Finally, the results obtained are used to interpret the L-shell absorption spectra of the two molecules.

PACS number(s): 33.70.Ca, 33.80.Eh, 34.50.Gb

I. INTRODUCTION

Core-level ionization from $2p$ inner shells in atomic systems give two spin-orbit components $2p_{1/2}$ and $2p_{3/2}$, with a statistical ratio 2:1 at photon energies well above the photoionization threshold. In the case of molecular photoionization, the chemical environment of an atom affects the ionization energies of valence and core orbitals and, thus, subtler effects can be found in molecular spectra. One of these is the molecular field splitting of the spin-orbit components. Observation of such effects usually requires very high resolution that has only become available recently with the advent of high-resolution electron spectrometers and undulator x-ray sources. As a consequence, over the last decade there has been a considerable interest in electron emission from molecules with molecular field-split core levels, both experimentally and theoretically [1–20]. For instance, combined theoretical and experimental studies of the Cl $2p$ photoelectrons spectra of HCl and DCl demonstrated the existence of three spin-orbit components due to coupling between the molecular field (MF) and the spin-orbit (SO) interaction, $^2\Pi_{3/2}$, $^2\Sigma_{1/2}^+$, and $^2\Pi_{1/2}$, sometimes also denoted as $2p_{3/2,3/2}^{-1}$, $2p_{3/2,1/2}^{-1}$, and $2p_{1/2,1/2}^{-1}$, respectively [11,19]. In addition to MF effects, the relativistic wave functions for core-excited neutral states are also controlled by singlet-triplet exchange (STE), which lifts the degeneracy among the $2l+1$ components of the shell [9], inducing fluctuations in the spin-orbit branching ratio. It has been shown that high-resolution molecular field and spin-orbit-split photoelectron spectra can be a sensitive probe of the molecular environment [12]. Despite a core-hole lifetime of one tenth of an eV for the chlorine $L_{2,3}$ holes, direct experimental evidence of fine-structure splitting induced by STE is difficult to obtain via x-ray absorption measurements because the linewidth is enlarged due to the Franck-Condon (FC) envelope. Thus in order to access information available from atomic $2p$ inner-shell populations in molecular spin-orbit components relevant to the nature of

chemical bonds, a reduction or quenching of the Franck-Condon broadening is necessary.

Resonant inelastic x-ray scattering (RIXS) in the 2–10 keV energy range has recently experienced a growing interest in isolated atoms and molecules [21–24]. As reported by Simon *et al.* [22] and Carniato *et al.* [25], measurements of KL lines using RIXS take advantage of the ultrafast dynamics and high-energy-resolution decay spectra with long-pulse light sources using the concept of effective duration time of the scattering process [26,27]. In this case, dynamical broadening caused by the Franck-Condon distribution is quenched on top of the photoabsorption resonance, where the width of the KL line approaches the core-hole lifetime (Γ_c).

Using the polarimetry capabilities of our x-ray spectrometer, we have recently measured the polarization of x-ray photons emitted in molecular core-to-core transitions accompanying KL x-ray emission [28]. In this study, spectra of core-excited neutral molecules were collected for HCl on the $1s \rightarrow 6\sigma^*$ resonance and for CF_3Cl on the $1s \rightarrow 11a_1^*$ resonance ($h\nu \sim 2823.5$ eV in both cases). We measured the KL emission corresponding to the filling of the core hole by a $2p$ core electron following the core-hole excitation. We have observed linear dichroism in the polarized x-ray-emission spectra and showed that this effect is sensitive to coupling between the MF and SO interactions.

In this paper, we detail the analysis of experimental data and computation of the electronic states and x-ray emission spectra of CF_3Cl and HCl. It is organized as follows: in Sec. II, we describe and discuss our theoretical approach and detail the computational techniques. In Sec. III, we describe the experimental scheme and in Sec. IV we present the experimental and theoretical results obtained on the KL emission spectra of gas-phase CF_3Cl and HCl. Section IV A shows how the analysis of polarization-dependent RIXS spectra with the help of theory leads to a direct determination of the electronic $2p_{x,y,z}$ populations in inner-shell orbitals. In Sec. IV B, we evaluate the effects of nuclear dynamics during the

core-hole lifetime on the RIXS profiles and on the determination of electronic populations. In Sec. V, we interpret the $2p$ absorption spectra of both molecules in light of the results obtained in KL emission. Finally, Sec. VI includes a short discussion on the origin of the effects observed.

II. THEORETICAL CONSIDERATIONS

The electronic ground state of HCl can be written in $C_{\infty v}$ symmetry notation as

$$(1\sigma)^2(2\sigma)^2(3\sigma)^2(1\pi)^4(4\sigma)^2(5\sigma)^2(2\pi)^4(6\sigma)^0,$$

where 6σ is the lowest-unoccupied orbital. The chlorine $1s$ atomic orbital corresponds to the 1σ orbital. CF_3Cl is tetrahedral and belongs to the C_{3v} symmetry point group. While it is convenient to use the atomic-orbital notation for the localized inner shells,

$$(Cl\ 1s)^2(F\ 1s)^6(C\ 1s)^2(Cl\ 2s)^2(Cl\ 2p)^6,$$

we use the proper C_{3v} notation for the outer shells,

$$(6a_1)^2(3e)^4(7a_1)^2(8a_1)^2(4e)^4(9a_1)^2(5e)^4(6e)^4(1a_2)^2(10a_1)^2$$
$$\times(7e)^4(11a_1)^0.$$

The $11a_1$ state is the lowest-unoccupied orbital. The Cl $1s$ core orbital corresponds to the $1a_1$ molecular orbital in C_{3v} notation. After resonant excitation of a Cl $1s$ core electron, radiative KL emission leaves the molecule in a core-excited state: $2p^{-1}11a_1^1$ for CF_3Cl and $2p^{-1}6\sigma^1$ for HCl. In the case of $2p$ core ionization, the relativistic wave function is built on nonrelativistic doublet states separated in energy by the combined influences of the MF and SO splittings. In the case of core excitation resulting in a $2p$ hole, the energetic structure of the final $2p^{-1}$ core-excited states is mainly determined by the spin-orbit splitting of the core shell, the molecular field, and the triplet-singlet exchange energy, which contributes to lift the degeneracy of the $2l+1$ components of the subshell. Due to the spin-orbit interaction, the relativistic wave function is a strong mixture of singlet and triplet states.

In the present study, all of the relevant potential-energy surfaces (PESs) are calculated *ab initio*. For CF_3Cl, the ground-state potential-energy surface along the C-Cl bond is represented by a Morse potential, $D_e(1-e^{-\beta(R-R_0)})^2$, with parameters D_e=3.755 eV, β=0.851 Å^{-1}, R_0(C-Cl)=1.752 Å, as given by Hahndorf *et al.* [29], yielding vibrational frequencies of 470 cm^{-1}, close to experiment (476 cm^{-1}). For HCl, we used the PES described in [22].

In the case of CF_3Cl, direct calculations of Franck-Condon factors face the difficulty that stretching of the C-Cl bond in the dissociative $(1s)^{-1}$ core-excited state can be accompanied by deformation of the CF_3 radical. Consequently, both the one-dimensional dissociative mode along the C-Cl bond and the CF_3 "umbrella" deformation, including six vibrational modes, must be considered simultaneously. In this case, the vibrational wave functions of the umbrella in the dissociated state can be written as the product of six-dimensional harmonic oscillators, with different frequencies, displaced from the ground-state equilibrium position along each normal mode. The analytical approach we used is based

on the expression for the overlap between two harmonic oscillators with ω_k'/v_k' (vibrational core-hole state) and ω_k/v_k =0 (vibrational ground state), where k denotes the vibrational mode, ω as the frequency, and v' as the vibrational level associated with this mode. The relations take care of the frequency relaxation of the final state. The calculated analytical $FC(\omega_k',v_k;\omega_k,0)$ Franck-Condon factors are collected in [30].

In order to determine Franck-Condon factors, we also need to calculate the change in normal coordinate between the neutral ground state and the core-excited state. In principle, this can be done in a straightforward manner. In this study, we used the approach proposed by Thomas *et al.* [31]. A technique particularly well adapted to cases where a change in geometry occurs upon core excitation. This method has recently proven to be very successful for studies of nitrile systems [32,33] and the water molecule [30].

The electronic wave functions for the dissociative states have been calculated using a one-dimensional Hamiltonian model that can be written as

$$H = -\frac{\hbar^2}{2\mu}\frac{d^2}{dr^2} + V(R_{Cl}), \tag{1}$$

where μ is the reduced mass of the system and $V(R_{Cl})$ is the vibrational potential along the H-Cl or C-Cl bond. The eigenvectors and eigenvalues were obtained by diagonalizing the Hamiltonian using the finite-difference approximation [34].

A. Computational details

1. Basis sets

All the calculations were performed using the GAMESS (US) *ab initio* program [35]. Geometry optimizations and harmonic frequencies for neutral initial and Cl $(1s)$ core-excited states are performed at the density-functional theory (DFT) level with the Becke three-parameter hybrid exchange [36] and the Lee-Yang-Parr gradient-corrected correlation functional [37] (B3LYP). At the DFT level, an IGLOO [38] basis set augmented by diffuse functions for Cl was used to properly describe the electron correlations of the neutral as well as the relaxation-correlation effects for the inner-shell core-excited states of HCl and CF_3Cl. For relativistic post-Hartree-Fock spin-orbit calculations, a flexible larger basis set (aug/cc/pCVQZ) [39] for Cl was used to describe the electronic relaxation and correlations and spin-orbit coupling in inner-shell core-excited states. In HCl, a similarly large aug-cc-pCVQZ was considered for H. With both the basis sets, the carbon and fluorine atoms were described by a 6–311 G polarized basis set with a $[4s,3p]$ contraction [40], with the addition of a special diffuse valence-Rydberg basis set $(\zeta_{s,p}=0.04380/0.01312;\ \zeta_d=0.2080/0.0690)$ for carbon atoms and $(\zeta_{s,p}=0.1076)$ for fluorine atoms, respectively.

2. Nonrelativistic calculations

The nonrelativistic dissociative Cl $(1s)^{-1}$ and Cl $(2p)^{-1}$ core-excited PES for HCl and CF_3Cl are computed in triplet and singlet forms at a restricted open-shell Hartree-Fock (ROHF/DFT) DFT level of theory, with the Kohn-Sham

scheme using a hybrid B3LYP correlation-exchange functional. The application of DFT to core-excitation phenomena takes advantage of the fact that both relaxation and correlation effects are simultaneously described at a moderate computational cost compared to self-consistent field and post-Hartree-Fock methods.

Although the DFT method is rigorous only for the ground state and it is a widely accepted practice to use it for core-hole or core-excited states calculations. Using DFT, the variational principle can be applied to densities referring to any state with fractional occupancy. For singlet core-excited state calculations, a local modified version of GAMESS was used. The excitation energies of the core-excited singlet states are calculated using the Kohn-Sham approach in combination with the sum method of Ziegler *et al.* [41]. The DFT calculations were performed in both cases at different representative H-Cl or C-Cl interatomic distances, ranging from 1.1 to 6.0 Å.

3. Relativistic calculations

The low-lying $2p^{-1}val^*$ SO components, including non-relativistic states for CF_3Cl and HCl at equilibrium bond lengths (1.75 Å and 1.28 Å, respectively), were calculated *ab initio*. The SO interaction, including the full Breit-Pauli coupling [42–44] integral package in GAMESS (US) [35], was used for calculations of the $(2p)^{-1}$ core-excited states. Spin-orbit-coupling calculations were performed on variational configuration-interaction (CI) wave functions dubbed SO-CI. In such a procedure, a model Hamiltonian in the complete active-space configuration-interaction (CAS-CI) basis is built and diagonalized to produce spin-mixed states, which are linear combinations of the complete active-space CI states. The Hamiltonian matrix is a sum of spin-free terms and spin-orbit terms $H = H_{sf} + H_{so}$. For SO-CI, the matrix H_{sf} is diagonal in the CAS-CI state basis, with the LS-coupled CAS-CI energies as the diagonal elements, and H_{so} contains only off-diagonal couplings between these LS states. The CI active space includes the three occupied $2p_{x,y,z}$ inner shells and the 80 lowest-unoccupied virtual orbitals, all derived from the nonrelativistic $2s^{-1}val^*$ potential. The core-excited reference wave function was represented by a generalized $2s^{-1}val^*$ singlet state to avoid orientational effects artificially induced in the calculations using $2p_{x,y,z}^{-1}val^*$ states. Because the $2s$ and $2p$ orbitals are close in energy ($\Delta E \sim 70$ eV [45]), similar relaxation effects are expected.

B. Diffusion factors

In general, the spectral and polarization properties of resonant x-ray scattering are guided by the doubly differential cross section [46],

$$\frac{d^2\sigma}{d\omega_1 d\omega_2} = \sum_f |F_f(\omega_1, \vec{e}_1, \vec{e}_2)|^2 \delta(\omega_1 - \omega_2 - \omega_{fo}), \quad (2)$$

where ω_1, $\vec{e}_1$ and ω_2, $\vec{e}_2$ are the frequencies and polarization vectors of the incoming and outgoing photons, respectively. The transition energy from the ground state to the final core-excited state is denoted as ω_{fo}. The transition matrix elements are given by

$$F_f^{\alpha\beta} = \sum_c \frac{\langle f|\mathcal{D}_\alpha|c\rangle\langle c|\mathcal{D}_\beta|o\rangle}{(\omega_1 - \omega_{cf}) + i\Gamma_c/2}, \quad (3)$$

where o is the initial ground state, c is the core-excited state, and f is the final state. The x, y, and z components of the dipole operator $\mathcal{D}$ are represented by α and β. The R dependence of the dipole transition moments between the initial state i and the final state j allows $D_{i,j}$ to be written as

$$D_{i,j} = \langle \Psi_{nucl}^j(R)|\mathbf{d}(\mathbf{R})|\Psi_{nuc}^i(R)\rangle, \quad (4)$$

where

$$d(R) = \langle \Psi_{el}^j(r,R)|\mathbf{d}|\Psi_{el}^i(r,R)\rangle. \quad (5)$$

The lifetime broadening of the neutral core-excited state is Γ_c, and $\hbar\omega_{cf}$ is the transition energy between this state and the final state f. For KL emission after Cl $1s$ excitation, c has a hole in the Cl $1s$ orbital and an excited electron in the $6\sigma^*$ orbital for HCl or $11a_1^*$, for CF_3Cl, and can be written generally as $1s^{-1}val^*$. The final state f has a hole in the $2p$ inner shell and an excited electron in a valence orbital and can be written $2p_\gamma^{-1}val^*$. In our case, formula (3) takes the simple form

$$F_{2p_\gamma^{-1}val^*}^{\alpha\beta} = \sum_c \frac{\langle 2p_\gamma^{-1}val^*|\mathcal{D}_\alpha|1s^{-1}val^*\rangle\langle 1s^{-1}val^*|\mathcal{D}_\beta|o\rangle}{(\omega_1 - \omega_{cf}) + \iota\Gamma_c/2}. \quad (6)$$

Due to SO coupling, the $2p_\gamma^{-1}val^*$ final states are linear combinations of triplet and singlet nonrelativistic components,

$$2p_\gamma^{-1}val^* = \sum_S C_\gamma^z 2p_z^{-1}val^* + \sum_T C_\gamma^{x,y} 2p_{x,y}^{-1}val^*$$
$$+ \sum_S C_\gamma^{x,y} 2p_{x,y}^{-1}val^* + \sum_T C_\gamma^z 2p_z^{-1}val^*, \quad (7)$$

where $2p_z^{-1}$ or $2p_{x,y}^{-1}$ denote a hole in one of the three $2p_{x,y,z}$ orbitals. The $2p_z$ orbital lies along the symmetry axis. For randomly oriented molecules, the mean-squared amplitude of diffusion is given by [47,48]

$$\langle |F_{2p_\gamma^{-1}val^*}|^2\rangle = A\lambda_{2p_\gamma^{-1}val^*}^{\alpha\alpha\beta\beta} + B\lambda_{2p_\gamma^{-1}val^*}^{\alpha\beta\alpha\beta} + C\lambda_{2p_\gamma^{-1}val^*}^{\alpha\beta\beta\alpha}. \quad (8)$$

The coefficients A, B, and C depend only on the polarization of the incident and emitted beams $\vec{e}_1$, $\vec{e}_2$,

$$A = -|\vec{e}_1 \cdot \vec{e}_2|^2 + 4|\vec{e}_1 \cdot \vec{e}_2^*|^2 - 1,$$

$$B = -|\vec{e}_1 \cdot \vec{e}_2|^2 - |\vec{e}_1 \cdot \vec{e}_2^*|^2 + 4,$$

$$C = 4|\vec{e}_1 \cdot \vec{e}_2|^2 - |\vec{e}_1 \cdot \vec{e}_2^*|^2 - 1,$$

with

$$\lambda_{2p_\gamma^{-1}val^*}^{\alpha\alpha\beta\beta} = \sum_{\alpha=x,y,z} \sum_{\beta=x,y,z} F_{2p_\gamma^{-1}val^*}^{\alpha\alpha} F_{2p_\gamma^{-1}val^*}^{\beta\beta*},$$

$$\lambda_{2p_\gamma^{-1}val^*}^{\alpha\beta\alpha\beta} = \sum_{\alpha=x,y,z} \sum_{\beta=x,y,z} F_{2p_\gamma^{-1}val^*}^{\alpha\beta} F_{2p_\gamma^{-1}val^*}^{\alpha\beta*},$$

$$\lambda_{2p_\gamma^{-1}val^*}^{\alpha\beta\beta\alpha} = \sum_{\alpha=x,y,z} \sum_{\beta=x,y,z} F_{2p_\gamma^{-1}val^*}^{\alpha\beta} F_{2p_\gamma^{-1}val^*}^{\beta\alpha*}.$$

Because the symmetry of the initial state is $^1\Sigma^+$ for HCl($C_{\infty v}$) and $^1A_1$ for CF$_3$Cl (C_{3v}), $\langle 1s^{-1}val^*|\mathcal{D}_\beta|o\rangle$ vanishes for $\beta = x, y$. Furthermore, if the final state has a core hole in $2p_z$, the $\langle 2p_z^{-1}val^*|\mathcal{D}_{x,y}|1s^{-1}val^*\rangle$ terms vanish. If the final state has a core hole in $2p_{xy}$, only the terms $\langle 2p_{xy}^{-1}val^*|\mathcal{D}_{x,y}|1s^{-1}val^*\rangle$ do not vanish. It follows that

$$\lambda_{2p_{xy}^{-1}val^*}^{\alpha\alpha\beta\beta} = \lambda_{2p_{xy}^{-1}val^*}^{\alpha\beta\beta\alpha} = 0,$$

and

$$\lambda_{2p_{xy}^{-1}val^*}^{\alpha\beta\alpha\beta} = F_{2p_{xy}^{-1}val^*}^{xz} F_{2p_{xy}^{-1}val^*}^{xz*} + F_{2p_{xy}^{-1}val^*}^{yz} F_{2p_{xy}^{-1}val^*}^{yz*}.$$

Noting θ is the angle between the photon polarization vectors $\vec{e}_1$ and $\vec{e}_2$, we obtain the final expression,

$$\langle |F_{2p_\gamma^{-1}val^{*+1}}|^2 \rangle = 2(1 + 2\cos^2\theta)[F_{2p_z^{-1}val^*}^{zz} F_{2p_z^{-1}val^*}^{zz*}]W_\gamma^z + 4(2$$
$$- \cos^2\theta)[F_{2p_x^{-1}val^*}^{xz} F_{2p_x^{-1}val^*}^{xz*}]W_\gamma^x. \quad (9)$$

We introduce W_γ^z and $W_\gamma^{x,y}$ as the nonrelativistic singlet $2p_z^{-1}val^*$ and degenerate $2p_{x,y}^{-1}val^*$ populations in the $2p_\gamma^{-1}val^*$ relativistic configuration. This formula explicitly includes polarization dependencies for the $2p_{x,y}$ and $2p_z$ components and governs the experimental approach we have used.

III. EXPERIMENTAL SCHEME

A. Emission pattern

Molecular K-shell photoabsorption processes leading to discrete states, i.e., resonant excitation, are intrinsically anisotropic because the photoexcited states have definite symmetries. This anisotropy is reflected in the angular distribution of the products created either from the initial core-hole state or from the states following the rapid decay of the initial state. As was discussed in the early publications by Dill and co-workers [49], processes such as electron ejection, fluorescence, and photodissociation bear the vestige of the symmetry of the initial excited state. For randomly oriented samples, such as gas-phase molecules, the orientation distribution is isotropic. However, because dipole selection rules impose symmetry restrictions in absorption, excitation of a core electron to an unoccupied molecular state by a monochromatic and polarized photon beam selects from a random ensemble molecules preferentially aligned with respect to the electric vector of the incoming radiation.

Fano and Macek [50] and later Greene and Zare [51] developed a formulation of the polarization-dependent angular distribution of photon emission from atoms and molecules using a two-step model to describe the excitation and the subsequent radiative decay. In this description, the anisotropy resulting from the symmetries of the electronic states can be represented by an alignment tensor and a geometrical factor both determined by the rotational quanta of the excited and final states. The radiation pattern is fully characterized by the angular distributions and polarizations of the emitted

radiation. Simple expressions can be obtained for emission intensities detected either parallel $I_\parallel$ or perpendicular $I_\perp$ to the incident polarization vector [51],

$$I_\parallel(\chi) = I_0[1 + R(3\sin^2\chi - 1)], \quad (10)$$

and

$$I_\perp(\chi) = I_0[1 - R], \quad (11)$$

where I_0 is proportional to the total intensity in all directions and polarizations; χ is the angle between the emission direction and the incident polarization vector; R is the factor of polarization anisotropy defined as half the product of the alignment parameter and geometrical factor [52]. From these equations, it appears that the radiation pattern can be characterized by the polarization P measured at $\chi = 90°$ and given by [53]

$$P(90°) = 3R/(2 + R) = (I_\parallel - I_\perp)/(I_\parallel + I_\perp). \quad (12)$$

The experimental results discussed in this paper were obtained in the $\chi = 90°$ geometry to allow measurements of the polarization dependencies given by Eq. (9).

B. Setup

Measurements were done at the third generation synchrotron-radiation facility, the Advanced Light Source (ALS) in Berkeley, California, on bending magnet beamline 9.3.1, previously described elsewhere [54–56]. This beamline uses a double Si(111) monochromator and provides intense (10^{11} photons/s), monochromatic (0.4 eV at the Cl K edge), and over 99% linearly polarized photons. X-ray-emission spectra were acquired using the polarized-x-ray emission spectrometer end station of the beamline. This apparatus is a curved-crystal Rowland-circle spectrometer [57] consisting of a variable-radius Si(111) crystal mounted on an in-vacuum bender, and a commercial two-dimensional (2D) position-sensitive microchannel-plate resistive-anode detector from Quantar Technology Inc. © operated in clean vacuum with pressures lower than 10^{-6} Torr.

Figure 1 shows a sketch of the end station. The incoming linearly polarized photon beam from the monochromator is focused onto a gas cell (A). Compared to the previous setup [57], the gas cell has been modified to improve the source volume in order to reduce self-absorption due to the distance between the exit window and the incident photon beam [24]. The original commercial stainless-steel cube has been replaced by a $38 \times 38 \times 15$ mm^3 block cell with a 50° angled 3-mm-diameter clearance hole closed on both ends by 2 $\times 2 \times 200$ nm^3 silicon nitride (Si$_3$N$_4$) windows. Gas samples are maintained at a static pressure of typically 400 Torr. During data acquisition, the gas cell is tilted at 50° relative to the incoming photon beam. The upstream window serves both as entrance for the incoming photon beam and exit window for the emitted x rays. Thus, the useful length of the source volume seen by the spectrometer crystal is less than 1 mm, which we found to improve significantly the energy resolution of the spectrometer. The counting rate is preserved ($\sim$100 counts/s for KV emission) because the majority of the incoming photons are absorbed and emitted within the
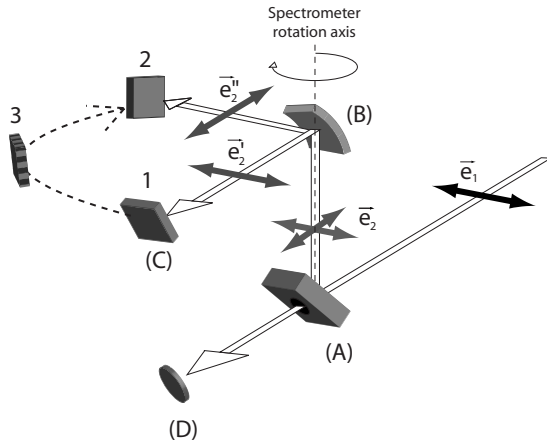
FIG. 1. Sketch of the polarized-x-ray emission spectrometer used on beamline 9.3.1 at the ALS (Berkeley, CA). (a) Gas cell. (b) Si(111) crystal. (c) 2D position-sensitive detector. (d) Silicon diode. (See text for details.)

first few millimeters of gas sample. A second Si_3N_4 window is used at the back of the gas cell and unabsorbed x-ray flux transmitted through the gas sample is measured using a Si photodiode (D) for relative absorption measurements.

While the gas cell and its housing stay fixed relative to the incoming photon beam, the secondary Si(111) crystal (B) can be rotated around the spectrometer axis containing the gas cell and the crystal. Extending from the crystal housing chamber is a 0.6-m-long arm leading to the detector housing that rotates with the crystal. The detector (C) is supported by a curved guide (not shown in Fig. 1) allowing the position of the detector to be moved along the Rowland circle to simultaneously change the Bragg angle of the spectrometer crystal and the energy range of the spectrometer. The detector collects a 20-eV-wide emission spectrum with ~ 0.5 eV resolution. At 2620 eV, for the Cl KL spectra, the Bragg reflection condition for Si(111) is fulfilled for 49°, and for Cl KL spectra near 2820 eV, at 44.6°, close to the x-ray Brewster angle of 45°. Consequently, contributions from x rays polarized perpendicular to the surface of the crystal are strongly quenched and a contribution of less than 2% is expected at 2625 eV for chlorine KL emission [58]. By rotating the spectrometer in the plane parallel to the incoming photon beam with respect to the incident polarization $\vec{e}_1$, the spectrometer acts both as a polarizer and an energy analyzer and we can analyze the polarization $\vec{e}_2$ of the emitted x rays from parallel to perpendicular, and all angles in between (positions 1,2, and 3 in Fig. 1, respectively).

IV. KL EMISSION SPECTRUM

Figure 2 (left panel) shows KL emission spectra measured on-resonance at 0° and 90° relative to the incident x-ray polarization. For both molecules, the measured values differ significantly from the statistical atomic $2p$ ratio (2:1). A clear polarization dependence is observed, with parallel polarization (0°) showing the largest deviation from the statistical ratio in each case. In addition, differences are observed between the two molecules. For CF_3Cl, the measured ratio for
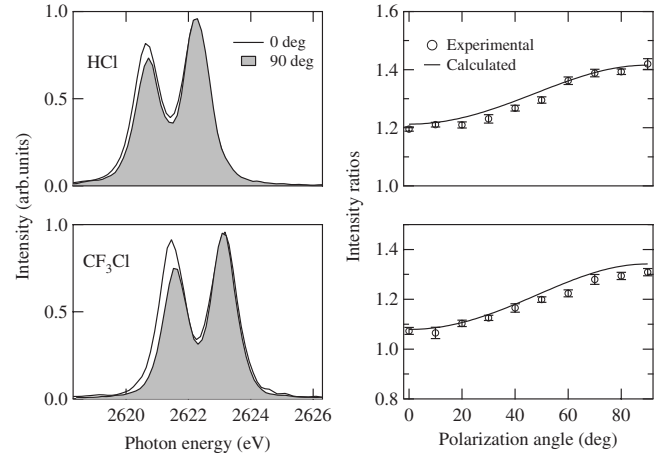

FIG. 2. Left: KL emission spectra measured on-resonance, Cl $1s \rightarrow 11a_1^*$ in CF_3Cl, and Cl $1s \rightarrow 6\sigma^*$ in HCl, for parallel (full line) and perpendicular (shaded) polarization with respect to the incident photon polarization. Right: experimental and calculated (curves) intensity ratios of spin-orbit components $2p_{3/2}/2p_{1/2}$ as a function of angle between the polarization vectors of the incident and scattered photons. The experimental ratios (circles) were obtained by fitting the two SO components to Voigt profiles. See text for calculation details.

perpendicular polarization vectors is $R_\perp = 1.30 \pm 0.05$. For parallel orientation, it is close to unity $R_\parallel = 1.07 \pm 0.05$. For HCl, we obtain $R_\perp = 1.42 \pm 0.05$ and $R_\parallel = 1.22 \pm 0.05$, respectively. The spectra also exhibit subtle changes in the apparent SO splitting as a function of polarization angle as shown in Fig. 2 (right panel). Although it could be possible to determine experimentally the parallel and perpendicular polarization components independently for each transition observed in the measured KL emission spectra by calibrating the transmission of the spectrometer at each angle, we simplify here the approach by deriving the ratio R between the two spin-orbit components $R = (2p_{3/2})/(2p_{1/2})$ at each angle. KL emission spectra were measured at ten different angles with respect to the incident polarization. The experimental ratios presented in Fig. 2 (right panel) were obtained by treating the spectra as atomiclike, i.e., simply fitting them to two Voigt profiles. The data are compared to the result of our *ab initio* calculations, which reproduce fairly well the angular dependence observed experimentally.

A. Spin-orbit components

We report in Tables I and II the energies (in cm^{-1}) and triplet and singlet populations of the $2p^{-1}11a_1^*$ spin-orbit components in CF_3Cl and $2p^{-1}6\sigma^*$ in HCl calculated at the equilibrium distances C-Cl (1.75 Å) and H-Cl (1.28 Å). The calculated spin-orbit splitting of the Cl $2p$ orbitals is ≈ 1.65 eV as observed experimentally. As indicated in the tables, each $(2p)^{-1}$ configuration splits into twelve sublevels, corresponding to $J_z = 2, 1, 0$, due to spin-orbit coupling, but only the six spin-orbit subcomponents including the singlet $2p_{x,y;z}$ populations contribute to the spectra. The $2p_x$ and $2p_y$ states for each spin-orbit peak are degenerate. The energy spacing between both the SOCI (IV-V) states in $2p_{3/2}$ is cal-

TABLE I. SO-CI calculated energies (in cm^{-1}) and triplet and singlet populations of $2p^{-1}$val* spin-orbit components in CF$_3$Cl (R=1.75 Å). Due to spin-orbit coupling, each $2p^{-1}$val* configuration splits into 12 sublevels, corresponding to J_Z=2,1,1,0. By symmetry constraints (see text), only the six $2p^{-1}$val* spin-orbit components including singlet $2p_{x;y;z}$ populations contribute to the spectra. The $2p_x$ and $2p_y$ states for each spin-orbit peak are degenerate.

Configuration	M_{J_z}	ΔE	Composition			
			$^3A_1$	^3E	$^1A_1$	^1E
			$(2p_{3/2}^{-1}-11a_1^1)$			
I	0	0	68%	32%		
II-1	1	56	59%	41%		
II-2	1	56	59%	41%		
III-1	2	295		100%		
III-2	2	295		100%		
IV-1	1	1122	12%	28%		60%
IV-2	1	1122	12%	28%		60%
V	0	3282		53.5%	46.5%	
			$(2p_{1/2}^{-1}-11a_1^1)$			
VI	0	13156	32%	68%		
VII-1	1	13660	30%	31%		39%
VII-2	1	13660	30%	31%		39%
VIII	0	15505		46%	54%	

culated to be 0.18 eV for HCl, while it is larger (0.27 eV) for CF$_3$Cl. For $2p_{1/2}$, the SO-CI (VII-VIII) energy splitting is theoretically estimated to be 0.14 eV for HCl and 0.23 eV for CF$_3$Cl.

Although our experimental setup does not provide sufficient energy resolution to resolve these energy spacings and the $2p_\gamma^{-1}val^*$ contributions to the nominal $2p_{1/2}$ and $2p_{3/2}$ spin-orbit components, it is possible to disentangle the ex-

TABLE II. SO-CI calculated energies (in cm^{-1}) and triplet and singlet populations of $2p^{-1}$val* spin-orbit components in HCl(R=1.28 Å). Due to spin-orbit coupling, each $2p^{-1}$val* configuration splits into 12 sublevels, corresponding to J_Z=2,1,1,0. By symmetry constraints (see text), only the six $2p^{-1}$val* spin-orbit components including singlet $2p_{x;y;z}$ populations contribute to the spectra. The $2p_x$ and $2p_y$ states for each spin-orbit peak are degenerate.

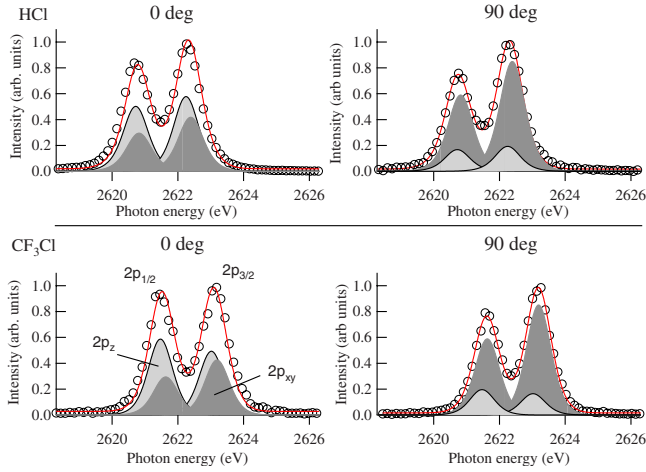| Configuration	M_{J_z}	ΔE	Composition			
			$^3\Sigma$	$^3\Pi$	$^1\Sigma$	$^1\Pi$
			$(2p_{3/2}^{-1}-6\sigma^1)$			
I	0	0	67%	33%		
II-1	1	25	54%	46%		
II-2	1	25	54%	46%		
III-1	2	112		100%		
III-2	2	112		100%		
IV-1	1	1009	16%	23%		61%
IV-2	1	1009	16%	23%		61%
V	0	2500		48%	52%	
			$(2p_{1/2}^{-1}-6\sigma^1)$			
VI	0	13077	33%	67%		
VII-1	1	13584	30%	31%		39%
VII-2	1	13584	30%	31%		39%
VIII	0	14728		52%	48%	

FIG. 3. (Color online) Experimental *KL* emission spectra (circles) obtained at 0° (left) and 90° (right) between the incident and emitted x-ray polarization vectors for HCl (top) and CF$_3$Cl (bottom). Solid curves are fits to the spectra. For each spin-orbit component, $2p_{1/2}$ and $2p_{3/2}$, two nondegenerate sublevels, $2p_z(^1A_1)$ (light gray) and $2p_{xy}(^1E)$ (dark gray), are included.

perimental data thanks to the angular behaviors of the components described in Eq. (9). First, theory indicates only the three nonrelativistic singlet $2p_{x,y,z}^{-1}$ subcomponents are nonvanishing, and two of them $2p_x^{-1}$ and $2p_y^{-1}$ are degenerate. Thus, it is sufficient to fit the $2p_{1/2}$ and $2p_{3/2}$ SO peaks with two subcomponents each, for a total of four per spectrum. Four-component fits were performed simultaneously on all ten spectra at the different polarization angles. Not only does this enhance the precision of the analysis, but it reflects the fact the underlying $2p_z$ and $2p_{x,y}$ contributions to the spectra are what drives the polarization dependencies observed in Fig. 2. The results are shown in Fig. 3 for the spectra obtained at 0° and 90°. For HCl, we find $2p_z$ contributes 54% to $2p_{3/2}$ and 46% to $2p_{1/2}$ ($2p_{x,y}$ contributes 59% and 41%, respectively). For CF$_3$Cl, we find $2p_z$ contributes 46% to $2p_{3/2}$ and 54% to $2p_{1/2}$. These experimentally derived populations are in very good agreement with our *ab initio* calculated populations reported in Tables I and II. The results collected for HCl, are also in very good agreement with the data obtained by Fink *et al.* [9].

Relative intensities and energy positions of the four components were varied in the multispectra fits, with the former (intensities) being the results of primary interest. Energy splittings between the $2p_z$ and $2p_{x,y}$ components obtained from the fits were 0.14 eV for HCl and 0.17 eV for CF$_3$Cl. In an attempt to determine the uncertainty in the splitting between the $2p_z$ and $2p_{x,y}$ molecular field components in the spectra, we ran the fitting procedure several times with different values for the splitting. Each time, we fixed the values in order to assess how sensitive the fits are to the exact splitting. The quality of the fits is mostly insensitive to the splitting, except for large excursions from the "best-fit" values. For example, relative to a best-fit value of 140 meV in HCl, changing the splitting by up to ±100 meV has little effect on the quality of the fit. Similarly, we ran the fitting procedure several times with different (but fixed) values of the relative intensities, in order to assess how sensitive the fits
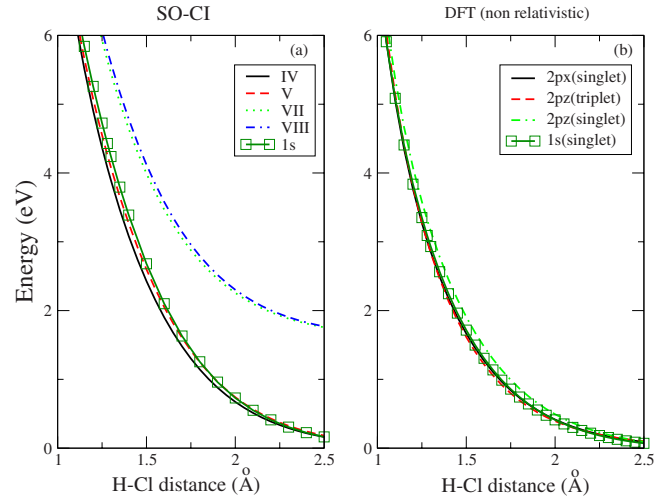

FIG. 4. (Color online) Theoretical HCl $1s^{-1}\sigma^{*1}$ and $2p^{-1}\sigma^{*1}$ potential-energy surfaces calculated at SO-CI (panel a) and DFT (panel b) level of theories. For SO-CI PES, Greek symbols reference to Table II.

are to the exact values. In contrast to the insensitivity to the splitting, the quality of the fits was found to be very sensitive to the relative intensities. The key findings of this work are the relative intensities of the $2p_z$ and $2p_{x,y}$ molecular field components, not their splitting. For example, relative to the best-fit values of 54% and 46% for the sharing of the total $2p_z$ contribution in the $2p_{3/2}$ and $2p_{1/2}$ spin-orbit peaks in HCl, changing the values by only 1% (e.g., to 55% and 47%) had a significant effect on the quality of the fit. Thus, the determination of relative populations from our measurements is actually quite sensitive.

The peak shapes and widths to use fitting the experimental spectra with four components were not known *a priori* and had to be calculated. The profiles used were derived from the calculation of the transition elements given in Eq. (6) for each molecule. Contrary to HCl, the first vibrational level ($v = 1$) of the ground state of CF$_3$Cl is populated at room temperature. The corresponding profile is calculated and summed with the profile obtained for $v = 0$ taking into account an expected ~10% population at 293 K. To first approximation, we assume the potential-energy surfaces of the $1s^{-1}val^*$ intermediate state and the various $2p^{-1}val^*$ final states are exactly parallel. For the systems studied in this work, parallel potentials are good assumptions and yield the same energy widths for all four components and, thus, this width was fixed in the fitting procedure. Nevertheless, in order to asses how nonparallel potentials affect the profiles used in the fit, we took a close look at the potential-energy surfaces for which the deviation from parallelism is at a maximum: the $2p_z^{-1}val^*$ and the $1s^{-1}val^*$ singlet states. In Fig. 4, the (SO-CI) spin-orbit components are shown including the $^1\Sigma$ and $^1\Pi$ nonrelativistic states along the H-Cl bond coordinates (panel a) compared with nonrelativistic DFT calculations (panel b). It is found that for CI and DFT approaches, the various PES of the $1s^{-1}val^*$ intermediate state and $2p^{-1}val^*$ components are not strictly parallel. To make a reasonable choice of a set of PES, i.e., DFT or CI, we show in Fig. 5 (panel a), the ground state (Morse potential) and
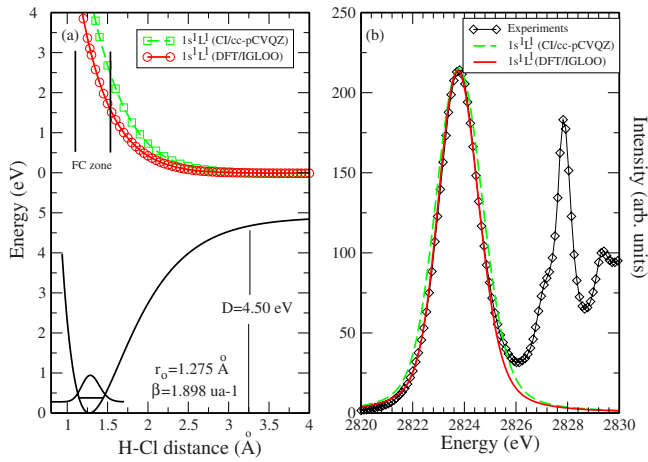
FIG. 5. (Color online) Panel (a) theoretical ground-state and $1s^{-1}\sigma^{*1}$ potential-energy surfaces calculated at SO-CI and DFT level of theories. Panel (b): experimental K-shell x-ray absorption spectrum of HCl compared with CI and DFT simulations.

$1s^{-1}val^*$ PES calculated at both the post-Hartree-Fock (CI) and DFT level. In the Franck-Condon zone, CI and DFT $1s^{-1}val^*$ calculated curves are not exactly parallel. In order to decide between DFT or CI PES, as a model to simulate RIXS profiles, we show in panel (b) the K-shell experimental x-ray absorption spectrum of HCl compared with theoretical simulations. As can be seen, the shape and full width at half maximum (FWHM ≈ 1.9 eV) of the experimental spectrum is perfectly reproduced with DFT, while the FWHM is overestimated with CI.

Overall, the effects of a small nonparallelism of the PES are found to be negligible, having only subtle effects in the tails and thus minor effects on the results. Therefore, we feel confident we are modeling the contributions to the spectra properly.

B. *R*-dependence of the spin-orbit ratios

As shown previously, nuclear dynamics can have an important influence on spectral features measured in molecular x-ray emission [22]. From *ab initio* calculations of the electronic state PES for both molecules, we can investigate theoretically the effect of varying internuclear distance R on the apparent spin-orbit ratio. The Franck-Condon zone for HCl stretches over roughly 0.50 Å, between 1.05 Å and 1.6 Å, while the FC window for CF$_3$Cl is smaller (≈ 0.3 Å between and 1.60 Å and 1.90 Å). From the $1s^{-1}val^*$ PES, we can extract the first derivative of the energy as a function of the internuclear distance around the equilibrium bond length. The corresponding average slopes are estimated to be -9.5 eV/Å for HCl and -10.5 eV/Å for CF$_3$Cl, respectively. The Cl $1s$ core-hole lifetime is ~ 1 fs [22]. The lengthening of the H-Cl or C-Cl chemical bond during the 1 fs core-hole lifetime is calculated by wave-packet propagation along the dissociative $1s^{-1}val^*$ PES for HCl and CF$_3$Cl as shown in Fig. 6 and is found to be ~ 5 pm for HCl and ~ 1 pm for CF$_3$Cl, respectively.

The DFT/B3LYP calculated singlet-triplet energy differences ΔST and SO-CI $2p_z$ populations, spin-orbit states V

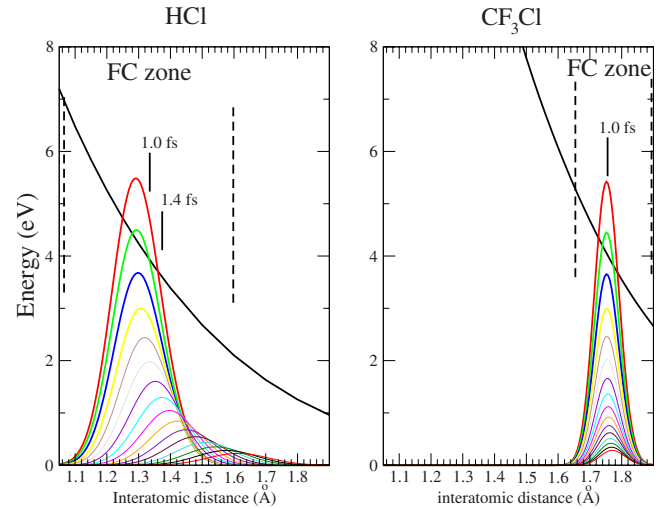FIG. 6. (Color online) Wave-packet propagation calculated along the dissociative $1s^{-1}val^*$ PES in HCl and CF$_3$Cl in the corresponding Franck-Condon region.

(see Tables I and II), as a function of the internuclear distance, are reported in Figs. 7 and 8, respectively. The results of the calculations indicate the strength of the splitting inside each spin-orbit component is sensitively dependent on the nature of the bond and interatomic distance between the chlorine atom and the ligand oriented along the chemical bond, which influences the mixing between triplet and singlet states caused by spin-orbit interaction. In particular, a larger singlet-triplet exchange energy along the X-Cl bond is evidenced for the $2p_z$ core orbital in comparison with the perpendicular $2px, y$ orbitals. The same effect is observed for both molecules. As seen in Fig. 8, at large internuclear distance between hydrogen and chlorine, or carbon and chlorine, the molecular field and singlet-triplet exchange effects are weakened and the nondegenerate components collapse into two spin-orbit components, while the quasiatomic split-
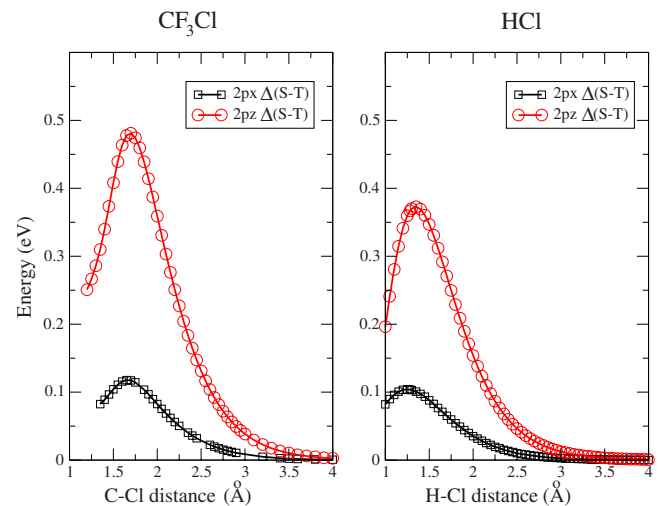

FIG. 7. (Color online) DFT/B3LYP [36,37] ΔST exchange energy of the $2p_{x,y,z}^{-1}val^{*1}$ states at the equilibrium bond lengths for HCl(1.28 Å) and CF$_3$Cl(1.75 Å). Singlet DFT theoretical values were estimated from the sum method of Ziegler *et al.* [41].
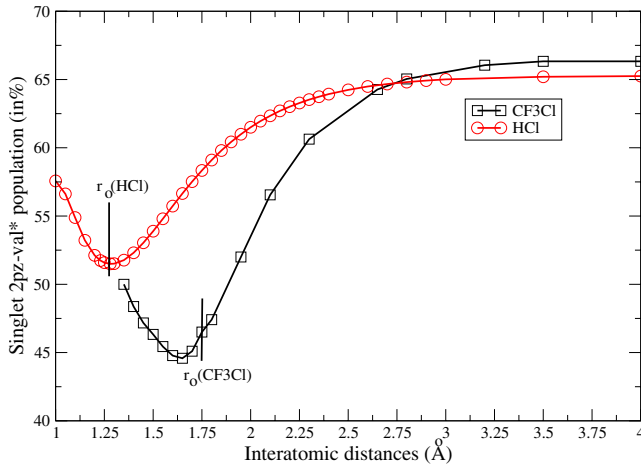
FIG. 8. (Color online) SO-CI population of the singlet $2p_z \rightarrow val^*$ state in the $2p \rightarrow val^*$ relativistic state (V) of HCl and CF3Cl as a function of interatomic distance.
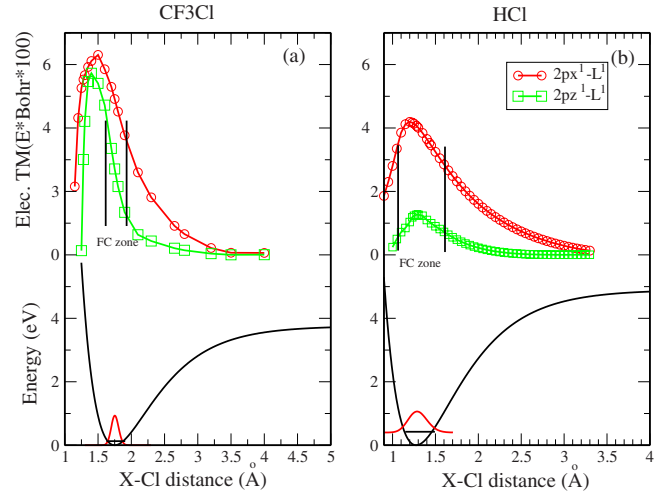

FIG. 9. (Color online) Electronic part of the transition moment between the ground state and the $2p_z val^*$ and $2p_{x,y} val^*$ final states as a function of the internuclear distance.

ting remains close to 1.6 eV. As long as the final nonrelativistic states do not differ in energy, the branching ratio between the total $2p_{3/2}$ and $2p_{1/2}$ states is found to be 2:1. The variation in the singlet $2p_z val^{*1}$ nonrelativistic state population (in %) reported in Fig. 8 presents a minimum in both cases. Its position is different for HCl(≈ 1.30 Å) and CF$_3$Cl(≈ 1.65 Å). In the case of HCl, the SO-CI population has a local minimum close to the equilibrium distance. Therefore, a small deviation of the H-Cl bond distance, from 1.275 Å to 1.37 Å, does not affect the SO-CI population. In the case of CF$_3$Cl, the nuclear motion is too small, from 1.75 to 1.80 Å, to affect the SO-CI population. As a consequence, we assume that the SO-CI populations are unchanged during the resonant scattering process.

V. $2p$ CORE-LEVEL ABSORPTION SPECTRA

Using the decomposition of the KL RIXS emission spectrum obtained above, we can calculate photoabsorption profiles at the Cl $2p$ edge (~ 200 eV). Following x-ray absorption at the L edge, only the $(2p)^{-1}(11a_1)^1$ relativistic states with $^1A_1$ or ^1E symmetry contributes to the oscillator strength in CF$_3$Cl because these states have nonzero dipole transition matrix elements with the $^1A_1$ ground state of the molecule. For HCl, only relativistic states with Σ and Π symmetry contribute to the oscillator strength. This simplifies the calculation of the oscillator strength f_{i-f}, which is given by

$$f_{i->f} = \frac{2}{3}(E_f - E_i)|\langle \Psi_f | \vec{r} | \Psi_i \rangle|^2, \qquad (13)$$

where E_i, E_i, Ψ_i, and Ψ_f are the energies, and the relativistic wave functions of the initial and final states, respectively. The photoexcitation strength to a given relativistic final state is, therefore, given by the transition probability to the nonrelativistic singlet $^1A_1(\Sigma)$ or degenerate $^1E(\Pi)$ components times its weight (population) in the relativistic configuration. This can be written as

$$f_{i->f} = \frac{2}{3}(E_f - E_i)|\langle \Psi_f^{nonrel} | \vec{r} | \Psi_i^{nonrel} \rangle|^2 |\langle \Psi_f^{nonrel} | \Psi_f^{rel} \rangle|^2 = \frac{2}{3}(E_f - E_i)I_{nr,f} \cdot I_{r,f} \qquad (14)$$

where Ψ_i^{nonrel} is the wave function of the nonrelativistic $^1A_1$ (Σ) or ^1E state (Π). In this equation, $(E_f - E_i)$ is two orders of magnitude greater than the energy shift between the two spin-orbit components $2p_{3/2}$ and $2p_{1/2}$. As a first approximation, the energy positions $(E_f - E_i)$ are considered constant over the whole Cl $2p$ absorption energy region.

We now consider the intensity values $(I_{r,f})$, which describe how the total nonrelativistic intensity $(I_{nr,f})$ is distributed among different relativistic states. The term $I_{nr,f}$ corresponds to the population W_γ^z or $W_\gamma^{x,y}$ of both singlet states $(2p_z)^{-1}(val^*)^1$ and $(2p_{xy})^{-1}(val^*)^1$ in relativistic components (γ=IV-V-VII-VIII) already given in Tables I and II. The second term $I_{nr,f}$ is the transition moment between the ground state and $(2p_z)^{-1}(val^*)^1$ and the $(2p_{xy})^{-1}(val^*)^1$ nonrelativistic components.

Figure 9 shows the calculated electronic part of the transition moments between the ground state and the $2p_z val^*$ and $2p_{x,y} val^*$ final states as a function of the internuclear distance. As can be seen in the figure, large variations are observed around the Franck-Condon regions for both molecules. To perform the calculation of the x-ray absorption spectra (XAS), we integrate simultaneously the variations in the vibrational and the electronic parts along the internuclear distances. It is interesting to note that in both cases HCl and CF$_3$Cl, the transition moment for the $2p_z \rightarrow$ lowest unoccupied molecular orbital (LUMO) excitation is more affected by the chemical bond than in the perpendicular (x,y) directions.

Calculated Cl $2p$ XAS are displayed in Fig. 10 for both HCl and CF$_3$Cl, together with total ion yields measured at the ALS using a magnetic spectrometer [59]. Very good agreement is obtained between theory and experiment for both molecules. As a consequence of the molecular field, the
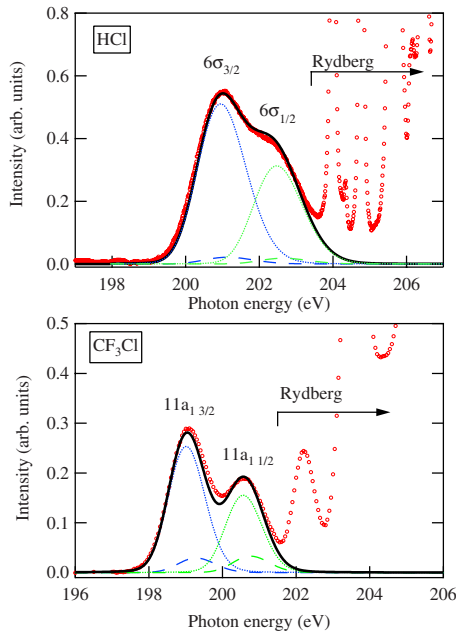
FIG. 10. (Color online) Comparison of the experimental and calculated x-ray absorption spectra at the $2p \to 6\sigma$ resonance for HCl and the $2p \to 11a_1$ resonance for CF_3Cl, below the $2p$ ionization threshold. Circles represent the experimental total ion yield. Dotted lines represent the calculated $2p_{x,y}val^*$ states contribution, and dashed lines represent the $2p_z val^*$ contribution, for each spin-orbit component.

theoretical intensity ratio $(I_{3/2}/I_{1/2})$ is estimated to be 1.442, in good agreement with the experimental value of 1.454, but far from the atomic statistical spin-orbit ratio 2:1. It should be noted that determination of the experimental ratio strongly depends on accurate measurements of the intensity ratio between the two $2p$ spin-orbit components. As can be seen from the calculations, especially for HCl, singlet $2p_{x,y} \to val^*$ components have much more intensity than those of singlet $2p_z \to val^*$. It is difficult to detect such structures with conventional measurements. Polarized-RIXS is thus a unique tool to evidence the nature, weight, and polarization dependence of such substructures and gives essential information to reconstruct x-ray absorption spectra.

VI. DISCUSSION

As seen in Fig. 3, the 0° spectra for HCl and CF_3Cl clearly have different spin-orbit ratios. Yet, our analysis reveals a difference in the $2p_z$ contributions to the two spin-orbit states of only 8%. The key result of this analysis is found in the observation that these results differ with molecules, indicating that the make up of each SO component depends on the chemical environment, including interatomic distance, and influences the mixing of triplet and singlet states caused by the SO interaction. To understand such variations in spin-orbit population from one molecule to another, we report in Fig. 11 the HF generalized valence bond theory (GVB) and DFT atomic Mulliken population as a function of bond length for HCl and CF_3Cl. At large distances, the final state has one electron localized on the hy-
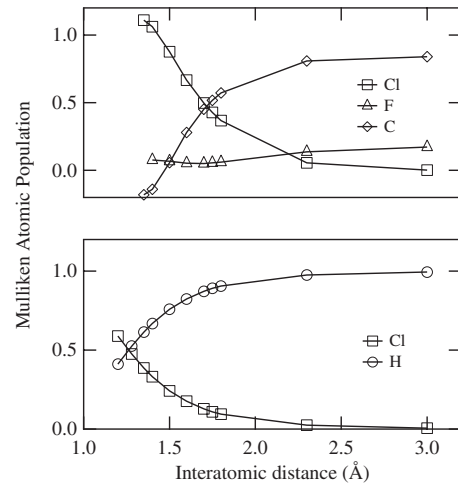

FIG. 11. Triplet DFT/B3LYP [36,37] and GVB (singlet) Mulliken atomic population of the LUMO* as a function of the bond length for CF_3Cl and HCl core excited in a $2p_z$ inner shell.

drogen atom in HCl or on the CF_3 fragment in CF_3Cl, an "atomic" chlorine with a hole in the $2p$ subshell and full occupancy of the valence levels. In this case, the singlet-triplet exchange energy vanishes while the population of the singlet $2p_z val^*$ configuration in the $2p_{3/2}$ spin-orbit component tends toward the atomic value (66%), as shown in Figs. 7 and 8. At shorter distances, the excited electron is transferred to the chlorine atom, while we observe in Fig. 8 an increase in the population of the singlet $2p_z val^*$ fifth $2p_{3/2}$ spin-orbit component. It is interesting to note that the core-excited chlorine atomic Mulliken population found for the LUMO is similar for HCl and CF_3Cl at their equilibrium distances.

As shown in Fig. 11 and Table III, the origin of the different populations in $2p_{x,y,z}$ between HCl and CF3Cl is not due to different charge densities between H and CF_3 but rather due to a different distribution of the LUMO electron density between valence and diffuse orbitals. Indeed, analysis of the results in Table III for HCl shows that the LUMO electronic density is mainly delocalized in a diffuse s orbital, i.e., far from the chlorine nucleus. On the contrary, for CF_3Cl molecule at $R_{C-Cl} = 1.75$ Å, the fractional electron density is mainly localized onto p and nd_{z^2} valence orbitals oriented

TABLE III. Localization onto diffuse or valence (s,p) of the atomic Mulliken population in the LUMO when $2p_z$-LUMO core excitation.

	s	p
	Valence/diffuse	Valence/diffuse
	CF_3Cl	
$R = 1.35$ Å	$-0.02/\mathbf{0.43}$	0.20/0.23
$R = 1.75$ Å	$-0.06/0.003$	0.20/0.02
	HCl	
$R = 1.28$ Å	$0.16/\mathbf{0.37}$	0.09/0.01

along the C-Cl bond length. At short C-Cl distance (R = 1.35 Å), the core-excited electron on the LUMO transfers to the chlorine atom. However, Fig. 7 shows that in this case, the electron density is repelled far from the nucleus toward diffuse s and p atomic orbitals, contributing to an attenuation of the corresponding singlet-triplet exchange energy. The delocalization into diffuse orbitals of the excited electron at short distances is, therefore, in some sense, equivalent to the electron transfer of the core-excited electron to the ligand at large distances. Therefore, the small differences between spin-orbit component in HCl and CF_3Cl probed by polarized RIXS reflect the subtle change in the chemical bond between the chlorine nucleus and the ligands.

VII. CONCLUSION

In conclusion, we have performed polarization-resolved resonant x-ray scattering measurements on HCl and CF3Cl in order to probe the effects of molecular field and singlet-triplet exchange on inner shells in neutral molecular systems. We observe linear dichroism in the spin-orbit doublet for both molecules after resonant Cl K-shell excitation. Although our experimental resolution does not energy resolve each in-dividual electronic state contributing to the spin-orbit doublets in the spectra, we take advantage of the symmetry properties of x-ray emission to disentangle their polarization dependencies. With the help of measurements taken at various polarization orientations with respect to the incident electric vector coupled with *ab initio* calculations, we obtain sensitive determinations of molecular $2p_z$ and $2p_{xy}$ populations in the spin-orbit doublets. The population analysis can be then used to interpret and calculate *ab initio* L-shell absorption spectra, which provided excellent agreement with experimental data. Finally, we note that the same effects have been observed in molecules such as CH_3Cl, Cl_2, and H_2S and that this method should be applicable to any molecular system, providing a unique probe of molecular effects on electronic structure.

[1] S. Svensson, A. Naves de Brito, M. P. Keane, N. Correia, and L. Karlsson, Phys. Rev. A **43**, 6441 (1991).

[2] S. Svensson, A. Ausmees, S. J. Osborne, G. Bray, F. Gel'mukhanov, H. Ågren, A. Naves de Brito, O.-P. Sairanen, A. Kivimäki, E. Nõmmiste, H. Aksela, and S. Aksela, Phys. Rev. Lett. **72**, 3021 (1994).

[3] M. R. F. Siggel, C. Field, L. J. Saethre, K. J. Børve, and T. D. Thomas, J. Chem. Phys. **105**, 9035 (1996).

[4] K. J. Børve, Chem. Phys. Lett. **262**, 801 (1996).

[5] K. J. Børve, L. J. Sæthre, and S. Svensson, Chem. Phys. Lett. **310**, 439 (1999).

[6] K. J. Børve, L. J. Sæthre, J. D. Bozek, J. True, and T. D. Thomas, J. Chem. Phys. **111**, 4472 (1999).

[7] K. J. Børve and T. D. Thomas, J. Chem. Phys. **111**, 4478 (1999).

[8] R. Püttner, Y. F. Hu, G. M. Bancroft, H. Aksela, E. Nõmmiste, J. Karvonen, A. Kivimäki, and S. Aksela, Phys. Rev. A **59**, 4438 (1999).

[9] R. Fink, M. Kivilompolo, and H. Aksela, J. Chem. Phys. **111**, 10034 (1999).

[10] N. Kosugi and T. Ishida, Chem. Phys. Lett. **329**, 138 (2000).

[11] M. Kivilompolo, A. Kivimäki, M. Jurvansuu, H. Aksela, S. Aksela, and R. F. Fink, J. Phys. B **33**, L157 (2000).

[12] E. Kukk, J. D. Bozek, J. A. Sheehy, P. W. Langhoff, and N. Berrah, J. Phys. B **33**, L51 (2000).

[13] R. Püttner, V. Pennanen, T. Matila, A. Kivimäki, M. Jurvansuu, H. Aksela, and S. Aksela, Phys. Rev. A **65**, 042505 (2002).

[14] R. F. Fink, F. Burmeister, R. Feifel, M. Bässler, O. Björneholm, L. Karlsson, C. Miron, M.-N. Piancastelli, S. L. Sorensen, H. Wang, K. Wiesner, and S. Svensson, Phys. Rev. A **65**, 034705 (2002).

[15] A. Giertz, M. Bässler, O. Björneholm, H. Wang, R. Feifel, C. Miron, L. Karlsson, and S. Svensson, J. Chem. Phys. **117**, 7587 (2002).

[16] T. Matila, R. Püttner, A. Kivimäki, H. Aksela, and S. Aksela, J. Phys. B **35**, 4607 (2002).

[17] N. Kosugi, J. Electron Spectrosc. Relat. Phenom. **137-140**, 335 (2004).

[18] M. Poygin, R. Püttner, M. Martins, V. Pennanen, M. Jurvansuu, Y. H. Jiang, H. Aksela, S. Aksela, and G. Kaindl, Phys. Rev. A **74**, 012711 (2006).

[19] O. Travnikova, R. F. Fink, A. Kivimäki, D. Céolin, Z. Bao, and M. N. Piancastelli, Chem. Phys. Lett. **426**, 452 (2006).

[20] O. Travnikova, R. F. Fink, A. Kivimäki, D. Céolin, Z. Bao, and M. N. Piancastelli, Chem. Phys. Lett. **474**, 67 (2009).

[21] P. A. Raboud, M. Berset, J.-Cl. Dousse, Y.-P. Maillard, O. Mauron, J. Hoszowska, M. Polasik, and J. Rzadkiewicz, Phys. Rev. A **65**, 062503 (2002).

[22] M. Simon, L. Journel, R. Guillemin, W. C. Stolte, I. Minkov, F. Gel'mukhanov, P. Sałek, H. Agren, S. Carniato, R. Taïeb, A. C. Hudson, and D. W. Lindle. Phys. Rev. A **73**, 020706(R) (2006).

[23] M. Kavčič, M. Žitnik, K. Bučar, A. Mihelič, M. Štuhec, J. Szlachetko, W. Cao, R. Alonso Mori, and P. Glatzel, Phys. Rev. Lett. **102**, 143001 (2009).

[24] M. Simon, L. Journel, R. Guillemin, W. C. Stolte, I. Minkov, F. Gel'Mukhanov, P. Sałek, H. Ågren, S. Carniato, R. Taïeb, A. C. Hudson, and D. W. Lindle, J. Electron Spectrosc. Relat. Phenom. **155**, 91 (2007).

[25] S. Carniato, R. Taïeb, R. Guillemin, L. Journel, M. Simon, and F. Gel'mukhanov, Chem. Phys. Lett. **439**, 402 (2007).

[26] F. Gel'mukhanov, P. Sałek, T. Privalov, and H. Ågren, Phys. Rev. A **59**, 380 (1999).

[27] F. Gel'mukhanov and H. Ågren, Phys. Rep. **312**, 87 (1999).

[28] R. Guillemin, S. Carniato, W. C. Stolte, L. Journel, R. Taïeb, D. W. Lindle, and M. Simon, Phys. Rev. Lett. **101**, 133003 (2008).

[29] I. Hahndorf, E. Illenberger, L. Lehr, and J. Manz, Chem. Phys. Lett. **231**, 460 (1994).

[30] S. Carniato, J. Chem. Phys. **126**, 224307 (2007).

[31] T. Darrah Thomas, L. J. Saethre, S. L. Sorensen, and S. Svensson, J. Chem. Phys. **109**, 1041 (1998).

[32] S. Carniato, V. Ilakovac, J. J. Gallet, E. Kukk, and Y. Luo, Phys. Rev. A **70**, 032510 (2004).

[33] S. Carniato, V. Ilakovac, J.-J. Gallet, E. Kukk, and Y. Luo, Phys. rev. A, **71**, 022511 (2005).

[34] J. Javanainen, J. H. Eberly, and Q. Su, Phys. Rev. A **38**, 3430 (1988).

[35] M. W. Schmidt *et al.*, J. Comput. Chem. **14**, 1347 (1993).

[36] A. D. Becke, J. Chem. Phys. **98**, 5648 (1993).

[37] C. Lee, W. Yang, and R. G. Parr, Phys. Rev. B **37**, 785 (1988).

[38] W. Kutzelnigg, U. Fleischer, and M. Schindler, *NMR Basic Principles and Progress* (Springer, Heidelberg, 1990), Vol. 23.

[39] D. E. Woon, T. H. Dunning, Jr., R. Seeger, and J. A. Pople, Chem. Phys. **98**, 1358 (1993).

[40] R. Krishnan, J. S. Binkley, R. Seeger, and J. A. Pople, J. Chem. Phys. **72**, 650 (1980).

[41] T. Ziegler, A. Rauk, and E. J. Baerends, Theor. Chim. Acta **43**, 261 (1977).

[42] T. R. Furlani and H. F. King, J. Chem. Phys. **82**, 5577 (1985).

[43] H. F. King and T. R. Furlani, J. Comput. Chem. **9**, 771 (1988).

[44] D. G. Fedorov and M. S. Gordon, J. Chem. Phys. **112**, 5611

[45] D. Céolin, M. N. Piancastelli, R. Guilllemin, W. C. Stolte, S.-W. Yu, O. Hemmers, and D. W. Lindle, J. Chem. Phys. **126**, 084309 (2007).

[46] J. J. Sakurai, *Advanced Quantum Mechanics* (Addison-Wesley, Reading, MA, 1967).

[47] Y. Luo, H. Ågren, and F. Gel'mukhanov, J. Phys. B **27**, 4169 (1994).

[48] Y. Luo, H. Ågren, and F. Gel'mukhanov, Phys. Rev. A **53**, 1340 (1996).

[49] S. Wallace and D. Dill, Phys. Rev. B **17**, 1692 (1978); D. Dill, J. R. Swanson, S. Wallace, and J. L. Dehmer, Phys. Rev. Lett. **45**, 1393 (1980).

[50] U. Fano and J. H. Macek, Rev. Mod. Phys. **45**, 553 (1973).

[51] C. H. Greene and R. N. Zare, Annu. Rev. Phys. Chem. **33**, 119 (1982).

[52] J. A. Guest, K. H. Jackson, and R. N. Zare, Phys. Rev. A **28**, 2217 (1983).

[53] S. H. Southworth, D. W. Lindle, R. Mayer, and P. L. Cowan, Phys. Rev. Lett. **67**, 1098 (1991).

[54] R. C. C. Perera, G. Jones, and D. W. Lindle, Rev. Sci. Instrum. **66**, 1745 (1995).

[55] G. Jones *et al.*, Rev. Sci. Instrum. **66**, 1748 (1995).

[56] http://www-als.lbl.gov/als/als_users_bl/9.3.1-Datasheet.pdf

[57] A. C. Hudson, W. C. Stolte, D. W. Lindle, and R. Guillemin, Rev. Sci. Instrum. **78**, 053101 (2007).

[58] S. Brennan, P. L. Cowan, R. D. Deslattes, A. Henins, D. W. Lindle, and B. A. Karlin, Rev. Sci. Instrum. **60**, 2243 (1989).

[59] W. C. Stolte, R. Guillemin, S.-W. Yu, and D. W. Lindle, J. Phys. B **41**, 145102 (2008).